




Full-Tracking Algorithm for Convective Thunderstorm System From Initiation to Complete Dissipation

Jianhua Yin¹ , Zengxin Pan^{2,3} , Daniel Rosenfeld^{2,3} , Feiyue Mao^{1,3} , Lin Zang⁴ ,
Yannian Zhu^{5,6}, Jiayi Hu⁷ , Jiangping Chen¹, and Jianya Gong^{1,3}

¹School of Remote Sensing and Information Engineering, Wuhan University, Wuhan, China, ²Institute of Earth Sciences, The Hebrew University of Jerusalem, Jerusalem, Israel, ³State Key Laboratory of Information Engineering in Surveying, Mapping, and Remote Sensing, Wuhan University, Wuhan, China, ⁴School of Electronic Information, Wuhan University, Wuhan, China, ⁵School of Atmospheric Sciences, Nanjing University, Nanjing, China, ⁶Joint International Research Laboratory of Atmospheric and Earth System Sciences & Institute for Climate and Global Change Research, Nanjing University, Nanjing, China, ⁷Cooperative Institute for Mesoscale Meteorological Studies, University of Oklahoma, NOAA/OAR National Severe Storms Laboratory, Norman, OK, USA

Key Points:

- A novel method is developed to track full components of deep convective systems (DCSs) from their initiation to total cirrus dissipation
- Lifetime of DCSs is extended by up to 10 hr, and their area is enlarged by 16% averagely after continuously tracking their detrained cirrus
- Integrated total rainfall amounts are comparably contributed between frequent but small and rare but large DCSs

Supporting Information:

Supporting Information may be found in the online version of this article.

Correspondence to:

Z. Pan,
pzx@whu.edu.cn

Citation:

Yin, J., Pan, Z., Rosenfeld, D., Mao, F., Zang, L., Zhu, Y., et al. (2022). Full-tracking algorithm for convective thunderstorm system from initiation to complete dissipation. *Journal of Geophysical Research: Atmospheres*, 127, e2022JD037601. <https://doi.org/10.1029/2022JD037601>

Received 5 AUG 2022
Accepted 25 OCT 2022

Abstract Accurate tracking of all components (including core, anvil, and cirrus) of deep convective systems (DCSs) throughout their lifecycle is key to quantifying their impacts on radiative forcing, especially of the anvil and cirrus. Here, a new Full-tracking Algorithm for Convective Thunderstorm System is developed based on geostationary satellite. It successfully tracks DCSs starting from the initial core to complete dissipation of cirrus detrained from them, and integrates all the related components that split from the initial convective core into a whole DCS. Results show that more than half of the tracked DCSs experience splitting evolutions, with an average of eight sub-cores during their lifetime. With tracking cirrus generated by DCSs, the lifetime of DCSs is lengthened by up to 10 hr, and their area is enlarged by 16% on average. Generally, long-lived DCSs have lower cloud top temperature, greater rainfall, and larger area, with more frequent splitting evolutions than short-lived DCSs. Additionally, DCSs always reach their peaks within 6 hr after initiation regardless of their lifetime. This paper provides a basis for further quantifying the evolution of DCS properties, their impacts on the global radiation budget, and the water cycle in the climate system.

1. Introduction

A deep convective system (DCS) produces frequent lightning and a large quantity of rainfall, thus playing an important role in regulating the regional water cycle and energy budget, especially in the tropics (Carey et al., 2005; L. M. Carvalho et al., 2002; Rasmussen et al., 2016; Roca et al., 2010). Previous studies showed that mesoscale convective systems, which are large cloud clusters of merged convective clouds, can contribute about 56% of total rainfall in the tropical area, even beyond 80% over land especially (Feng et al., 2021; Roca et al., 2014). Tracking the lifecycle of DCS is important to quantify the DCS effect on precipitation and Earth radiation budget (Prein et al., 2017; Taylor et al., 2017). Many DCS tracking methods, such as the area-overlapping, centroid, and cross-correlation methods, have been developed using satellites' infrared brightness temperature (BT) or radar reflectivity (Goyens et al., 2012; Hennon et al., 2011; Hu, Rosenfeld, Ryzhkov, et al., 2019; Rosenfeld, 1987).

Williams and Houze (1987) first used the area-overlapping method to track satellite-observed convective systems based on their sufficient overlapping area at successive moments. This initial area-overlapping tracking method is available for the simple DCS without the complicated fragmentation and merging evolutions. Additionally, many improved satellite-observed methods based on area overlapping have been developed to consider the fragmentation and merging in DCS lifetime, such as Tracking Of Organized Convection segmentation (TOOCAN; Fiolleau & Roca, 2013; W. Li et al., 2021), FLEXible object TRAcKeR (FLEXTRKR) and "Grab 'em, Tag 'em, Graph 'em" algorithms (Whitehall et al., 2015). For example, after identifying the coldest convection core, TOOCAN identified all the overlapping multiple convective cores in the timeline of the lifecycle as the same convective system. The FLEXTRKR method considers an overlapped small convection as a component of the mature convective system when it is short-lived below 6 hr (Feng et al., 2018). Furthermore, Rosenfeld (1987) first applied the area-overlapping method to tracking convection based on radar data, and it was further developed by Hu, Rosenfeld, Zrnicek, et al. (2019).

Additionally, the cross-correlation and centroid tracking methods are more often applied in tracking thunderstorm cells based on radar data (del Moral et al., 2018; Rinehart & Garvey, 1978; G. Wang et al., 2013; Zan et al., 2019). The cross-correlation algorithm divides the entire radar reflectivity map into small sub-domains and tracks them by finding the maximum correlation between them in consequent time steps (L. Li et al., 1995; Rinehart & Garvey, 1978; Tuttle & Foote, 1990). Although the cross-correlation algorithm estimates the small-scale convective cells inside the thunderstorm well, it cannot identify and track entire and independent systems, which contain convective core, stratiform anvils, and detrained cirrus. By contrast, the centroid tracking methods can better identify individual thunderstorm cells, typically as the Thunderstorm Identification, Tracking, Analysis, and Nowcasting (TITAN) method (Dixon & Wiener, 1993). The centroid on the radar signal (i.e., weight averaged radar reflectivity) is used to represent the convective cell, and then the optimal path of the centroid at continuous moments is identified to achieve deep convective tracking.

In the context of the increase in anthropogenic emissions and global warming, DCSs may become more frequent, intense, and variable globally (Koren et al., 2014; Liu & Zipser, 2015; Rosenfeld et al., 2008). Added aerosol emission significantly affects the microphysics, precipitation, and radiative forcing of DCS with large uncertainty (Koren et al., 2014; Pan et al., 2022, 2021; Rosenfeld et al., 2008). A complete DCS should begin with the initiation of a core and last until the dissipation of its related cirrus. It evolves during its lifecycle with the complicated processes of initiation, sometimes splitting and merging and total dissipation. Moreover, the whole DCS radiative forcing and related variations are determined by its whole coverage area and lifetime, especially for anvil and cirrus (Christensen et al., 2016; Feng et al., 2011; Hartmann & Berry, 2017). Tracking the cirrus outflow of DCS is essential due to its large radiative effects. Thus, the full components of DCS should include the cores with intense convection, anvil where convective activity weakens until stopped, and cirrus detrained from anvil. Additionally, DCSs can interact with each other by connecting and merging, resulting in ambiguous boundaries of DCSs. This represents new challenges for tracking full components (core, anvil, and cirrus) of DCSs from their initial to total dissipation, and quantifying the properties and radiative forcing of DCSs accurately.

Previous area-overlapping algorithms usually tracked and identified a DCS by following the largest convective core throughout its lifetime (Mathon & Laurent, 2001; Vila et al., 2008). This approach may cause a complete DCS to be incorrectly identified as multiple smaller DCSs, causing statistical biases in DCS properties and lifetime. Additionally, under the scene of a multiple-core convective cluster, the identification of the anvil affiliation to the connected cores should be clarified further. A whole DCS radiative forcing consists of the forcing from the core, anvil, and cirrus detrained from the DCS system. The cirrus detrained from DCS were possibly ignored in many tracking methods and observations, especially those based on radar (Han et al., 2009), resulting in incomplete tracking of the radiative properties of DCS. However, DCS-generated cirrus plays an important role in Earth's radiation budget with poorly known effects, although cirrus has an average of 20% coverage globally (Matus & L'Ecuyer, 2017; Sassen et al., 2009).

The present study addresses these deficiencies by introducing a novel DCS tracking method named "Full-tracking Algorithm for Convective Thunderstorm System" (FACTS). It tracks a DCS from initiation to complete dissipation and encompasses all clouds that split off it based on the high temporal-spatial resolution of METEOSAT second-generation (MSG) geostationary satellite and Global Precipitation Measurement (GPM) precipitation data. FACTS is the latest and further development on Hu, Rosenfeld, Zrnicek, et al. (2019) and Rosenfeld (1987), which is unique in combining all the splits and tracking the full DCS. Our method has two major advantages:

1. Integrating complex splits and mergers when tracking DCS, obtaining full sub-components of DCS throughout its lifetime.
2. Seamless, continuous tracking of cirrus detrained from DCS even after the convective core is dissipated, ensuring the integrity of DCS components and lifetime.

All ice-top clouds (referring to core, anvil, and cirrus) split from the same ancestor convective core are integrated into a full DCS, including multiple convective clouds and their cirrus. This method is a foundation for further evaluating DCS properties and their radiative effect. The specific methodology and statistical results are presented in Sections 2 and 3, respectively.

2. Data and Methodology

2.1. Data and Their Collocation

2.1.1. METEOSAT Second Generation

MSG images are taken by the Spinning Enhanced Visible and Infrared Imager (SEVIRI) sensor, which provides 12 spectral bands with 15 min resolution and covers the range from -81° to 81° in latitude and from -79° to 79° in longitude. The nadir spatial resolution is 3 km, except for partial coverage of 1 km high resolution in the visible band (Schmetz et al., 2002). SEVIRI measurements are the bases of comprehensive products, including cloud properties, humidity, ozone, land surface, and sea ice, with high temporal-spatial resolution. The other instrument onboard the MSG is the Geostationary Earth Radiation Budget (GERB), which will be used for quantifying the aerosol cloud-mediated radiative forcing in subsequent studies.

Here, cloud mask, cloud top height, and brightness temperature at 12 μm (BT12) band from MSG were used for DCS tracking. BT12 is almost the same as brightness temperature at 11 μm (BT11) at the convective core area, but is more strongly influenced by ice and water particle absorption. This cause the brightness temperature difference between 11 and 12 μm ($\text{BTD}_{11-12\mu\text{m}}$) of cirrus to be mostly positive (Lee et al., 2014; Platt & Harshvardhan, 1988; Strabala et al., 1994). Therefore, the BT12 is closer to the true physical temperature for semi-transparent ice clouds which constitute most of cirrus clouds (Inoue, 1987).

2.1.2. GPM and NCEP

The GPM mission is an international project for providing 3D global precipitation observation (Hou et al., 2014). It consists of one core observatory with precipitation radar and approximately 10 constellation satellites with passive microwave measurements. Before the launch of Core GPM in 2014, GPM Integrated Multi-satellite Retrievals for Global precipitation mission (IMERG) data are mainly based on Tropical Rainfall Measuring Mission (TRMM) precipitation observation. The mean absolute monthly bias for the estimated rainfall of TRMM only approaches 9% compared with rain gauge data sets (Huffman et al., 2007). By combining the retrievals from the space-born radar, microwave radiometers, and geostationary infrared observations, IMERG can provide the estimation of precipitation at a global coverage (Huffman et al., 2019; Kummerow et al., 2001, 2015). Additionally, the IMERG product is further corrected using monthly rainfall gauge measurements to improve the precipitation estimation (Huffman et al., 2019). Here, the IMERG product was selected for allocated precipitation for each DCS with a 30 min interval and a $0.1^{\circ} \times 0.1^{\circ}$ spatial resolution.

The National Centers for Environment Prediction final operational global reanalysis (NCEP-FNL) data are produced by the Global Data Assimilation System, which collects data from multiple sources, including global telecommunication system and satellites and ground-based observation. NCEP-FNL provides $1^{\circ} \times 1^{\circ}$ grid resolution data with a time resolution of 6 hr, and it contains 26 pressure layers from 1,000 hPa to 10 hPa in the vertical direction. Many previous studies have already proven the agreement among multiple reanalysis wind vector and ground-based truth (D. Carvalho et al., 2014; Dong et al., 2017). For example, Sivan et al. (2021) verified the accuracy of wind vector from multiple reanalysis data through a Stratosphere-Troposphere wind profiler radar located at Cochin of India. The NCEP reanalysis data have a good averaged correlation ($R = 0.72$) for wind vector at stratosphere and troposphere with the ground-based truth, especially for U wind with the 0.85 correlation. NCEP-FNL was used in this work for multiple parameter data, including geopotential height and wind speed.

2.1.3. Data Collocation

The data from multiple observation and analysis platforms were collected for cloud, precipitation, and wind, as listed in Table 1. Based on the nearest neighbor interpolation, all data were matched to the 9×9 km grid of GERB to facilitate the follow-up study for DCS radiation forcing. In statistics, the difference in observations is slight before and after resampling, as shown for BT12 (Figure S1 in Supporting Information S1). Rainfall data were obtained from GPM IMERG. Thus, MSG data consistent with GPM's time resolution (30 min) were selected for a more accurate precipitation allocation. Linear interpolation was used to match NCEP data (6 hr interval) to the same time (30 min) resolution. Cloud mask was initially obtained by MSG, and then cloud types were identified by combining MSG BT12 data with rainfall obtained from GPM IMERG. The cloud top height data were used to calculate the cloud motion vector with the matched cloud top wind vector from the NCEP reanalysis data. Observation and reanalysis data from -50°W to 50°E and -25°S to 25°N (shown as Figure S1 in Supporting Information S1) were used in 2012, when the GERB data were available, including full-month data for January,

Table 1
Data Used in the Analysis With Their Sources and Spatial Resolutions

| Source | Resolution | Parameters |
|-----------|---------------------|---|
| MSG | 3 × 3 km, 15 min | Brightness temperature at 12 μm (K); cloud mask |
| | 9 × 9 km, 15 min | Cloud top height (m) |
| GPM IMERG | 0.1° × 0.1°, 30 min | Rainfall rate (mm/h) |
| NCEP-FNL | 1° × 1°, 6 hr | Wind speed (m/s) |

May–July, November, and December, and first-half-month data of February and August. GERB data availability was described in the previous paper of Pan et al. (2021).

2.2. Methodology

Our method includes four steps, as illustrated in Figure 1 and summarized as follows: (a) Classification of clouds. BT12 and rain rate threshold are used to classify cloud pixels as convective core, anvil, cirrus, supercooled water, and warm water cloud, as in previous studies (Ai et al., 2016; Vondou et al., 2010; Zheng et al., 2018). (b) Bordering DCS and its components. The boundaries of DCS components are identified one-by-one, especially for each DCS of the complicated multiple-core convective cluster. (c) Ice-top cloud tracking with splitting and merging evolution. Each ice-top cloud (i.e., convective cloud and its cirrus outflow) is tracked throughout its lifetime from initiation to dissipation considering splitting and merging. (d) Combining components and reorganizing them into full DCS life cycles. After tracking, all related ice-top clouds are recognized based on the same ancestor core and reorganized to obtain the complete life cycle and components of DCS. The method is described in Sections 2.2.1–2.2.4.

2.2.1. Identifying Deep Convective Cloud

The BT threshold at 12 μm band for identifying the core was set as 235 K because this temperature was strongly correlated with tropical convective precipitation (Hanna et al., 2008; Rickenbach, 1998; K. Y. Wang & Liao, 2006). However, the core identification only based on BT may be interfered by high-level cirrus without rainfall, resulting in the misclassification of cloud type. Therefore, rainfall rate (>1 mm/hr) was used as an additional criterion for identifying the cores. This criterion distinguishes between the detected core and the anvil or cirrus, as done by Pan et al. (2021). The IMERG data has a high sensitivity to non-rain ice particles, which possibly overestimate the probability of weak rainfall (Cui et al., 2020; Hayden & Liu, 2021; Zhang et al., 2021).

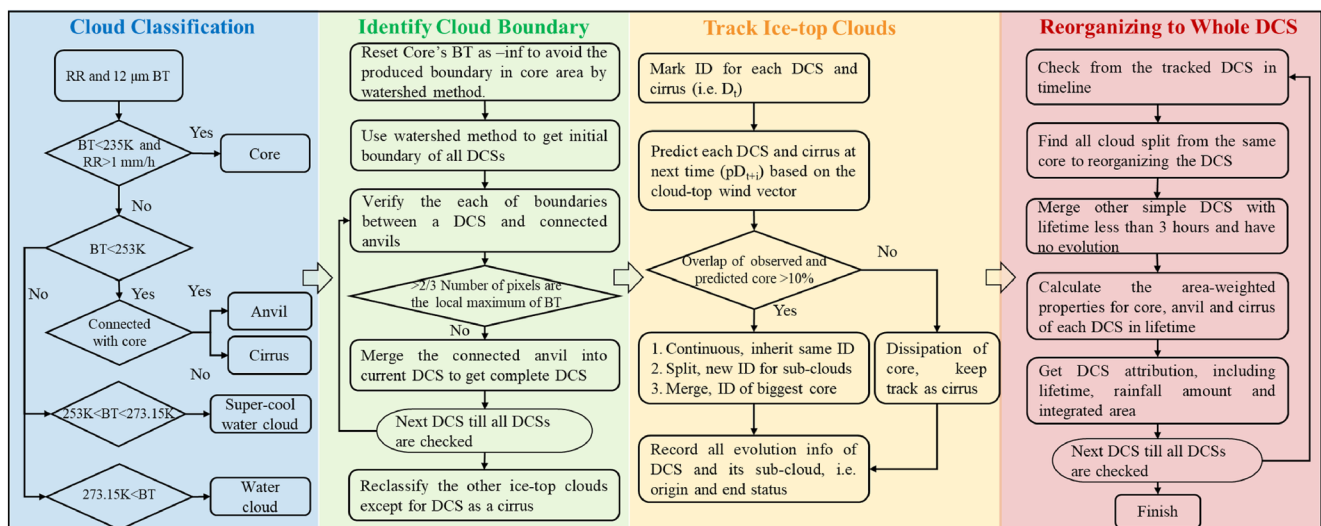


Figure 1. Step-by-step flow chart of the Full-tracking Algorithm for Convective Thunderstorm System (FACTS) tracking method. Deep convective system (DCS), brightness temperature (BT), and rainfall rate (RR).

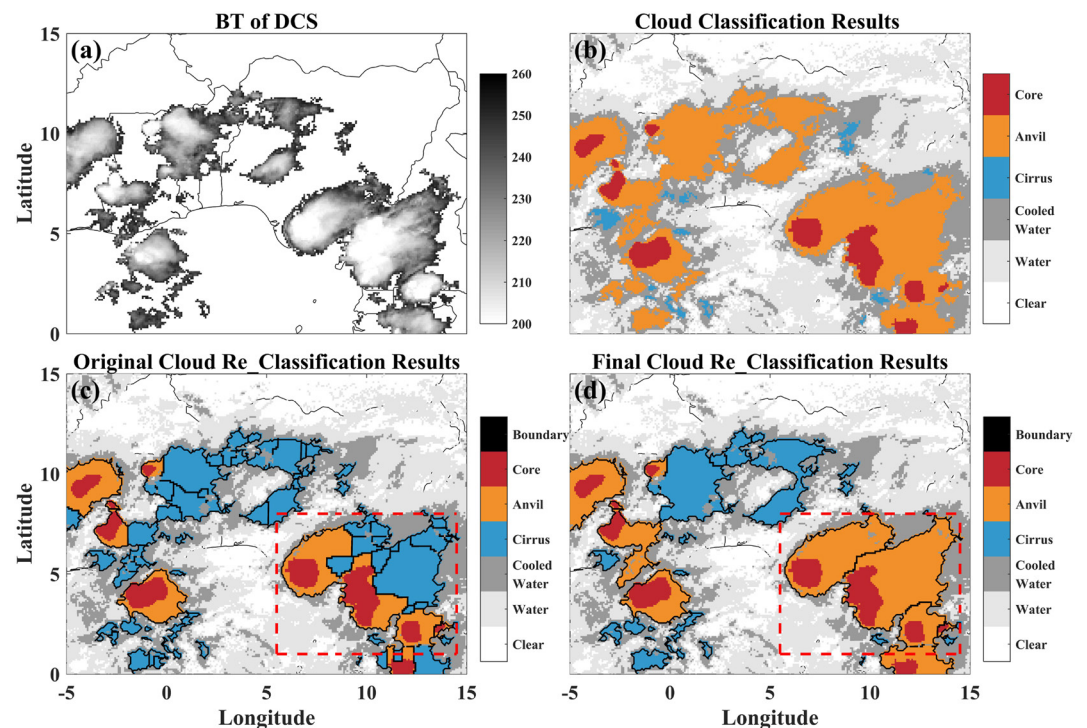


Figure 2. Comparison of results between original and improved watershed boundary recognition algorithm: (a) BT of deep convective system (DCS), (b) cloud classification before boundary identification, (c) preliminary DCS boundary and cloud reclassification, (d) improved DCS boundary and cloud reclassification after removing false boundary based on (c). The black lines represent the identified cloud boundaries.

The combined criteria of BT and rainfall rate for convective core are beneficial to constrain the effect of observed data uncertainty on cloud identifications.

Accurate anvil and cirrus allocation is necessary to determine the radiative characteristics of a DCS throughout its lifetime. A higher BT threshold (253 K) was used to identify the anvil and cirrus areas (Inoue et al., 2009). The difference between anvil and cirrus is whether it is connected to the detected core. Other clouds colder than 273.15 K are classified as supercooled water cloud and the residual clouds are classified as water cloud, which are not components of DCS. The detected core with an area of fewer than three pixels was removed to avoid the interference of very small clouds.

2.2.2. Bordering Each Convective Cloud and Its Components

The coverage of anvil and cirrus determines a DCS radiative forcing (Christensen et al., 2016; Feng et al., 2011; Hartmann & Berry, 2017). Accurate allocation of anvil and cirrus is conducive to a better quantification of the convective parameters and radiative forcing of DCSs. The identification of the anvil affiliation to the connected cores should be clarified further, especially under the scene of the multiple-core convective cluster. The watershed algorithm, which was first used for cell tracking by Rosenfeld (1987), is widely applied in boundary recognition (Hu, Rosenfeld, Zrnic, et al., 2019; Meyer, 1994). “Water” is poured into the pool defined from high to low BT (from the boundary to central core), forming a basin at the local minimum BT (core). The ridges, which are the local maximum of BT, are formed at the junction of adjacent “water basins.” For the convective system, such as a basin, the BT gradually increases from the core to the anvil boundary identified by the watershed method. Here, this approach can delineate the boundary between two adjacent anvils.

The BT usually changes irregularly at the top of DCSs (Figure 2a), which causes the watershed algorithm to identify many false boundaries and retain many fragmented anvil or cirrus as different entities (Figure 2c). Furthermore, with the evolution of convective systems, the multiple DCSs may coexist in the same convective cloud clusters with a connected boundary. A cloud boundary recognition algorithm for each DCS within multiple-core

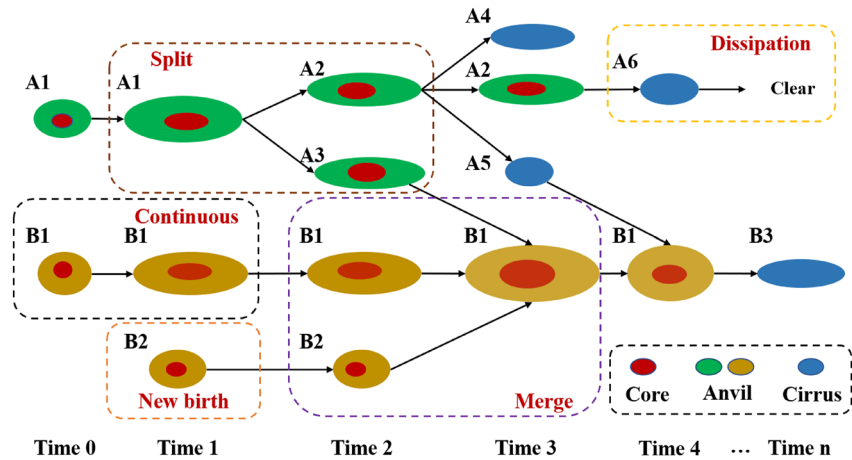


Figure 3. Evolution of all components of two tracked deep convective systems (DCSs; Systems A and B) throughout their life cycles. The full components of Systems A and B contain sub-cloud A1–A6 and B1–B3, respectively.

convective clusters was developed here based on the watershed algorithm, as shown in the second column of Figure 1, and summarized as follows:

1. Preliminary boundary is defined. The BT of the core is set as infinite because the core should not be divided by the watershed. The watershed algorithm can define the preliminary boundary (Hu, Rosenfeld, Zrnic, et al., 2019). However, many false boundaries can appear within the same cloud due to watershed over-segmentation, as a matter of course, cloud pixels with false boundaries to the convective core are identified to be cirrus as shown in red boxes in Figure 2c.
2. True boundary pixel is identified. The BT of boundary pixels should be the local maximum value within a small domain. Here, a boundary pixel is regarded to be true if its BT is a local maximum value in the longitudinal or latitudinal directions within a 5×5 pixels domain centered on it.
3. False boundaries are removed. Boundaries between the convective core and the adjacent anvil are iteratively checked. A boundary is defined as true if more than $2/3$ of boundary pixels are true based on the last step. Otherwise, the false boundaries are removed, and cirrus is reconnected to the convective core and identified as anvil again, as shown in the red box in Figures 2c and 2d.
4. All boundaries of convective clouds with adjacent anvils are iteratively checked, and false boundaries are removed. Then, the same processes in Steps 1–3 are initiated for all cirrus.

2.2.3. Tracking Ice-Top Cloud With the Evolution of Splitting and Merging

After marking the boundary for each ice-top cloud, its evolution is tracked by using the area-overlapping method with the further consideration of splitting and merging evolutions. The area-overlapping method has been widely used for convective system tracking and has achieved robust, continuous results. Due to the fact that this method may miss small clouds that are moving rapidly (Huang et al., 2018), the wind vector is used to predict the location of clouds at the next moment, improving the tracking of small clouds. Here, the evolution states of ice-top clouds can be new-birth, continuous, splitting, merging, and dissipation (Figure 3). New-birth and splitting produce new clouds, whereas the latter two statuses represent the end of the cloud. The tracking method for ice-top cloud is summarized in Figure 1 (light yellow panel) and shown as follows:

1. Each ice-top cloud i at time t ($I_{i,t}$) is predicted at the next time step (as $pI_{i,t+1}$) according to the matched wind vector from NCEP (Hall, 2004; Ocasio et al., 2020). The position of a convective core at the next time step is predicted by using the average wind vector from 1,000 to 500 hPa, whereas cirrus is predicted based on the wind vector at the cloud top height.
2. Convective clouds are tracked first based on the overlapping core area. The predicted position of convective cores at the next time step ($pI_{i,t+1}$) is compared with the actual position ($I_{i,t+1}$). To track fast, small convective clouds, the overlapping fraction is defined concerning the area of the smaller core. When the overlapping area of the core is larger than 10% between $pI_{i,t+1}$ and $I_{i,t+1}$, the inheritance and tracking of the core between the current and next time point are established.

3. Cirrus detrained from the convective clouds are continuously tracked after core dissipation until the total dissipation of the cirrus. The timeline of the ice-top clouds, including start (end) time, start (end) status, related ice-top cloud ID, and rainfall properties, is recorded.

We compared the DCS tracking results with the wind vector at different altitude levels (Figures S2a–S2c in Supporting Information S1), including averaged wind vector from cloud top, 500 hPa to cloud top, and 1,000–500 hPa. The results showed that tracking DCS with three different wind vectors results in almost the same convective trajectories with a similar total number of DCSs (Figures S2d–S2f in Supporting Information S1). Actually, the DCS motion is not very sensitive to the wind vector due to the relatively low overlapping area threshold (10%) used in the FACTS method.

2.2.4. Reorganizing Tracked Segments Into Complete DCS Throughout Their Lifetime

After finishing the ice-top cloud tracking, a complete DCS can be derived by sorting all relevant track segments of ice-top clouds derived from the same parent core. A complete DCS should begin with the initiation of a core and last until the dissipation of its related cirrus. Its record contains all related components, including the core, anvil, and detrained cirrus, considering splitting and merging. Incomplete record of the DCS components possibly generates a large uncertainty for DCS radiative effect due to the following causes:

1. Several small convective clouds split from the main DCS are missed when the main DCS is split. Instead, these small clouds are misclassified as a new initial DCS.
2. Cirrus detrained from convective clouds are usually ignored, but these cirrus can substantially affect radiative warming with a large cloud extent (Matus & L'Ecuyer, 2017).

Quantifying the whole DCS radiative effect depends on obtaining the complete evolution of the DCS throughout its lifetime, especially for its anvil and cirrus components. This method benefited from the complete record of ice-top cloud evolution information, backtracked to the core, anvil, and cirrus detrained from the same ancestor core to form the whole DCS. In Figure 3, cores A2 and A3 are split from A1, and cirrus A4 and A5 are detrained from A2. These clouds are from A1 and belong to parent System A. Furthermore, a large DCS (i.e., System B in Figure 3) may absorb the surrounding small, simple convective clouds (B2), which have not been split and with a short lifetime (no more than 3 hr). To ensure the integrity of this large system, even though the simple convective clouds (i.e., B2) do not come from this large DCS, it is still attributed to this system (i.e., B1).

Additionally, for the sub-convection and cirrus (i.e., A3 and A5), they should belong to their parent convective system from which they split off. If the residual cirrus and sub-convections of a previous system merge into a new system with a new convective core, they are ended. Simultaneously, these residual cirrus clouds and sub-convections (i.e., A3 and A5) merge with the new large system (i.e., System B) at this moment. Here, we use the observed and identified parent cores to identify the total number of DCSs. Therefore, the splitting and merging evolutions of cirrus and sub-convections have no effect on the total number of tracked DCSs. Additionally, this process for cirrus actually keeps the identity of all the cirrus detrained from convections, which is beneficial to accurately quantify the radiative forcing of DCSs in statistics.

3. Tracking Results of the FACTS Method

3.1. Case Analysis of a DCS Throughout Its Lifetime

Figure 4 shows the entire evolution of one 14.5 hr DCS case (named System A) above the ocean tracked by our FACTS method. It consists of eight identified sub clouds from A1 to A8. The initial core was identified at 04:30 UTC on 2 November 2012. In the initial phase of DCS, core A1 developed rapidly. Simple convective core A2 was born at 05:30 UTC and merged into A1 at 06:00 UTC. The merged DCS continued moving westward. Then, cirrus appeared for the first time at 11:30 UTC, as identified by the boundary recognition algorithm. The core dissipated completely at 13:30 UTC, and the DCS was fully determined to be cirrus. Finally, the cirrus dissipated at 19:00 UTC, which meant the end of the whole DCS lifetime.

Figure 5 shows the evolution of the properties of the DCS shown in Figure 4 throughout its lifetime. The BT of the core reached the lowest (Figure 5a) with the initiation of the rainfall at the core area (Figure 5d), then gradually increased from 203 to 220 K with increasing rainfall. This result indicates that the DCS reached the highest altitude just with rainfall initiation. The BT of the convective core was lower than that of the anvil. The BT

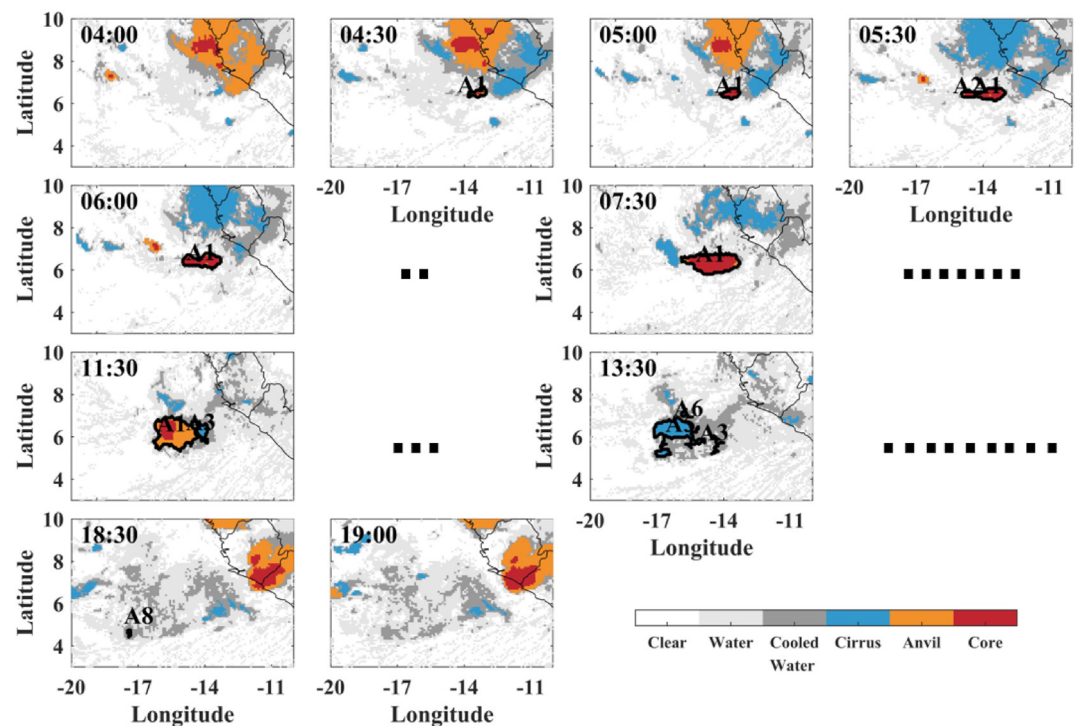


Figure 4. Tracked deep convective system (DCS; System A) throughout its lifetime (14.5 hr) from UTC 04:30 to 19:00 on 2 November 2012. Red, yellow, and blue represent the core, anvil, and cirrus, respectively. The boundary of the DCS System A is in black. The number of points represents the number of skipped time steps in the figure.

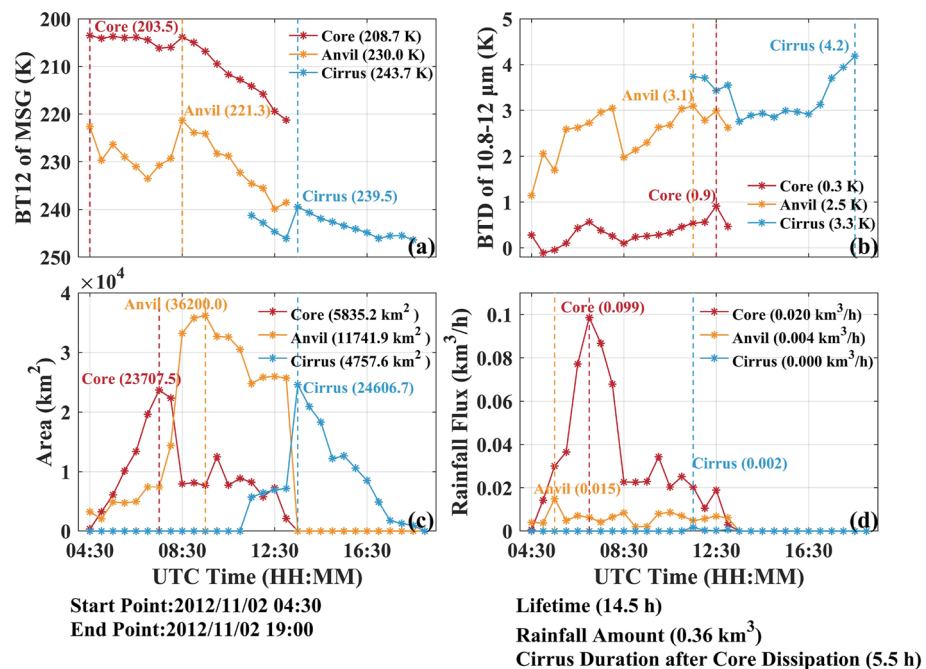


Figure 5. Evolution of deep convective system (DCS; shown in Figure 4) characteristics throughout its lifetime. (a) BT at 12 μm ; (b) BT difference of 10.8 minus 12 μm ; (c) area and (d) rainfall flux of its core, anvil, and cirrus. The rainfall flux of DCS is equal to rainfall rate times area. The numbers in the legend represent the mean value during the whole lifetime. The vertical dotted lines represent the time of peak, and the corresponding numbers indicate the peak values of DCS characteristics during the entire lifetime.

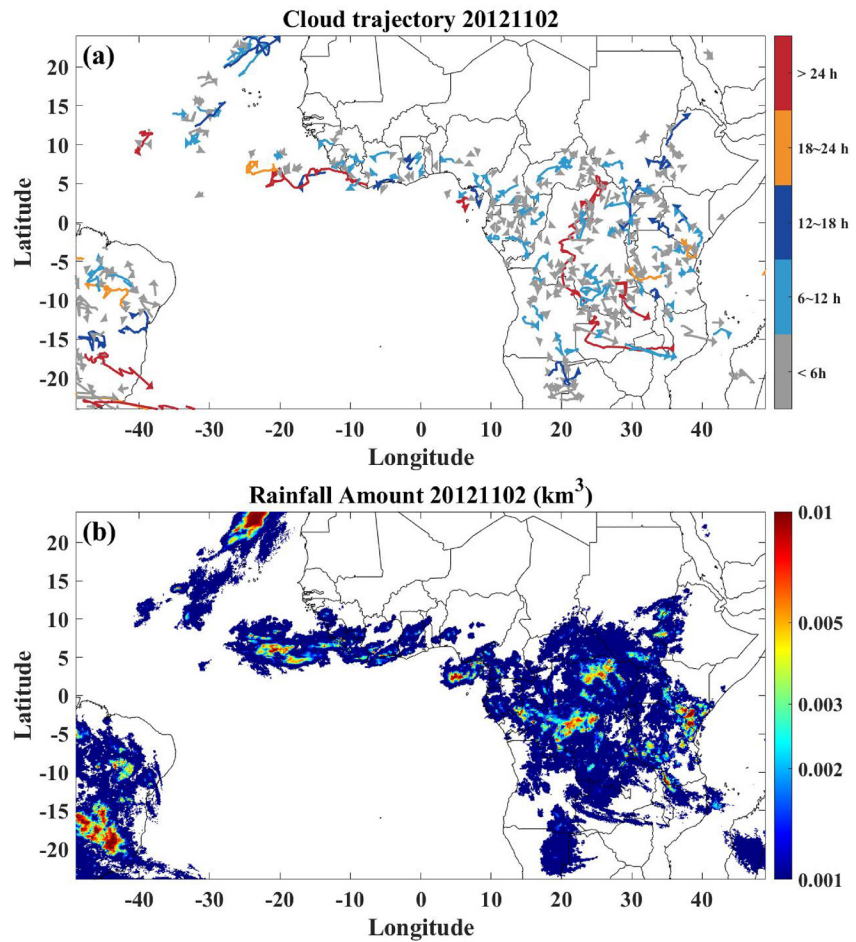


Figure 6. A tracking case of deep convective systems (DCSs) over a large domain started on 2 November 2012, including (a) all tracking trajectory lines with their lifetime shown by the colors and (b) integrated rainfall amount of DCSs. The tracking trajectory line of a DCS connects the center points of the DCS at each time step, and the arrow represents the direction of the DCS movement at the last time step.

difference between 10.8 and 12 μm (BTD of 10.8–12 μm) of the anvil was much higher than that of the core due to their thinner optical depth. Similarly, cirrus had higher BT and BTD than anvil (Figures 5a and 5b). The area and rainfall flux of the core (Figures 5c and 5d) were used to distinguish the initiation, maturation, and dissipation stages of the DCS. Rainfall flux was calculated as area multiplied by rainfall rate in the unit of km^3/h . The total rainfall amount of this DCS (0.36 km^3) was obtained by integrating the rainfall flux over the entire life cycle (14.5 hr). Additionally, cirrus always prevailed and remained for 5.5 hr after core dissipation with large size (up to $25,000 \text{ km}^2$) but very minimal precipitation.

Figure 6a shows the trajectories of all DCSs on 2 November 2012. Different lines represent the tracks of DCSs based on their central point in the system throughout their lifetime. Most DCSs have a short lifetime. Consistent with wind direction, the DCSs in West Africa moved westward, whereas the DCS in central Africa moved eastward. Figure 6b shows the precipitation distribution by DCS on 2 November of 2012, which amounted to 99 km^3 over the whole domain.

3.2. Statistics of Tracked DCS Characteristics

Based on our FACTS method, ~91,200 DCSs initially produced ~15,100 km³ of rainfall, tracked from -50°W to 50°E and -25°S to 25°N (as the domain at Figure 6) in 2012. To more accurately describe the evolution law of the convective system, we only retained the convection of the complete period, defined by the following criteria:

1. The too short-lived DCSs (core duration ≤ 1 hr) are removed. These DCSs contribute to 75% (~68,800) of total tracked DCS but only 6% (~900 km³) of total rainfall amount. A system is considered to have a full lifetime tracking when it starts with an increasing trend of rainfall and ends with a decreasing trend. Many of these tracked short-lived DCSs cannot achieve a complete evolution possibly due to the 30-min time interval of GPM IMERG, which is not sufficiently fine, possibly resulting in bias for larger DCSs.
2. Continuous DCSs cases that are misidentified as independent DCS (~420 cases and ~3,400 km³ rainfall) are removed. A case is defined as continuous multiple DCSs when the core of previous DCS is not totally dissipated when the new DCS starts at the same place. As shown in Figure S3 in Supporting Information S1, when the trough between two peaks of DCS core rainfall flux was less than 50% of the lower peak, the identified case contained actually two continuous DCSs, rather than one long-lived DCS with multiple rainfall peaks and a long lifetime.
3. Incomplete DCSs but with core duration > 3 hr (~9,600 cases and ~2,000 km³ rainfall) are removed. When a convection merged into other bigger mature system, if this convection lifetime is short (core duration ≤ 3 hr), it will be judged to one part of the mature system because it is generally small, as shown as the convection of B2 in Figure 3. However, if this convection has a longer lifetime (core duration > 3 hr), it is considered as an independent but incomplete DCS. This DCS does not dissipate normally, and should not be used to statistically analyze the DCS evolution during its whole lifetime.

Finally, 12,404 DCSs were obtained with the whole life cycle, producing a total of 8,700 km³ rainfall. Figure 7a shows the average rainfall amount of DCSs at intervals of 6-hr lifetime. 38% and 77% of the DCSs had lifetimes of ≤ 6 or ≤ 12 hr, respectively, with a low rainfall amount per DCS (red line in Figure 7a). With the increase in DCS lifetime, the average rainfall amount increases exponentially. However, due to the large number of short-lived DCSs, the integrated rainfall amount at each interval of DCS lifetime are comparable with each other (blue line in Figure 7a). Previous studies indicated that the IMERG data possibly overestimate the probability of weak rainfall, generating false rainfall in anvil regions (Cui et al., 2020; Hayden & Liu, 2021; Zhang et al., 2021). This may result in the overestimation of the rainfall amount of the tracked DCSs. Figure 5 shows that the rainfall amount is dominated by rainfall in core areas, while the rainfall in broad anvil areas contributes little to the total rainfall amount of DCSs. However, the contribution of the overestimated weak rainfall is still uncertain, and need to be further quantified and corrected in future.

One of the main advantages of our method is the seamless continuous tracking of cirrus detrained from DCS even after the convective core is dissipated. Cirrus and anvil are non-negligible warming factors to the Earth-atmosphere system (Matus & L'Ecuyer, 2017). Figure 7b shows core duration and cirrus duration after core dissipation. Cirrus duration after core dissipation increases with DCS lifetime and does not exceed 10 hr on average regardless of the DCS lifetime (Figure 7b). Similarly, the area of all DCS components increases with the DCS lifetime, especially for anvil (Figure 7c). Cirrus enlarges the average DCS area by 16% (blue line), and the anvils contribute 58% of the DCS area.

Another advantage of FACTS is the integration of the mergers and splits of a DCS throughout its life cycle. The findings reveal that more than half (7,185 out of 12,404) of the tracked DCSs have splitting or merging for their core during their lifetime. These evolving DCSs contained 57,749 sub-cores (Figure 8a). These tracked DCSs contained eight sub-cores on average, reaching up to 100, which were previously identified as different independent convective systems (Chen et al., 2019). More than one-third of DCSs (38%) had up to three sub-cores within 8 hr of their average lifetime (Figure 8a). Long-lived DCSs tend to split into more sub-cores than short-lived DCSs (red and grey bars in Figure 8a). Only ~2% of DCSs had more than 50 sub-cores with an average lifetime of 41 hr. It indicates that long-lived systems occur with a low probability but many sub-cores. Figure 8b shows the probability distribution function of rainfall amount for the complete convective system and their sub-cores (i.e., convective splits), which are possibly misidentified as new convection without the consideration of splitting evolutions. Results show the median rainfall amount had more than an order of magnitude difference (0.3 and 0.01 km³) between the DCSs with and without consideration of splitting evolution, respectively (Figure 8b). This difference is large because a full DCS consists of 8 sub-cores on average.

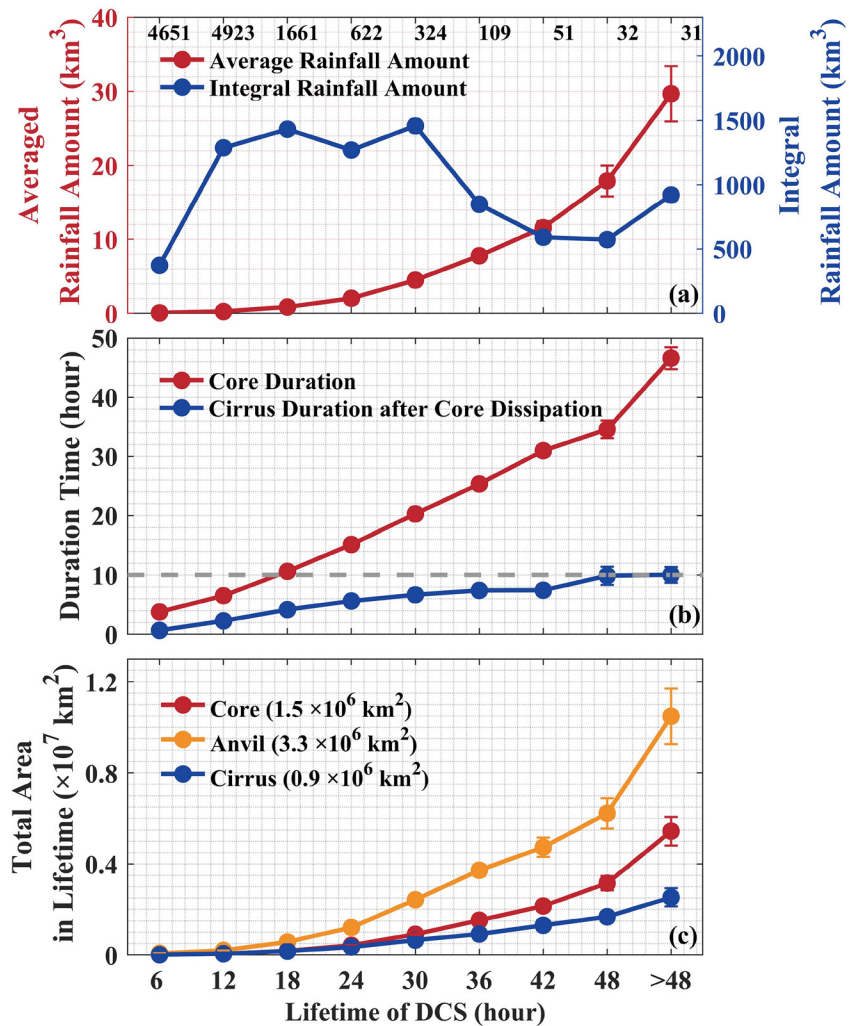


Figure 7. Evolution of deep convective system (DCS) characteristics at six-hour intervals of DCS lifetime, including (a) average and integral rainfall amounts, (b) core duration and cirrus duration after core dissipation, and (c) time-integrated area of different DCS components in their whole lifetime. The I-type vertical bars indicate the standard error of the DCS characteristics.

Figure 9 shows the changes of DCS characteristics from initial core to dissipation of related cirrus, including BT of core, rainfall flux, and core and anvil plus cirrus area. DCSs were divided into different classifications at 6 hr intervals of lifetime. Figure 9a shows that DCSs with a longer lifetime are on average characterized by lower core BT, indicating a stronger convective intensity. BT of core peak decreases by 1 K on average for every six-hour increase of DCS lifetime. Additionally, most short-lived DCSs reach the coldest (highest in altitude) point around 1 hr after initiation, consistent with a previous study (Feng et al., 2012). The time may be much shorter than 1 hr because the short-lived convective cloud with a core duration ≤ 1 hr was deleted. No matter how strong the DCS is, it will reach the coldest point near 6 hr at the latest. A longer-lived DCS has a slower change of BT during dissipation time. Figures 9b and 9c show the evolution of rainfall flux and core area for DCSs of different durations. The rainfall flux reaches the maximum shortly before the core area reaches its maximum near the half-lifetime point. The summed area of the anvil and cirrus at the peak time is more than twice that of the core (Figure 9d).

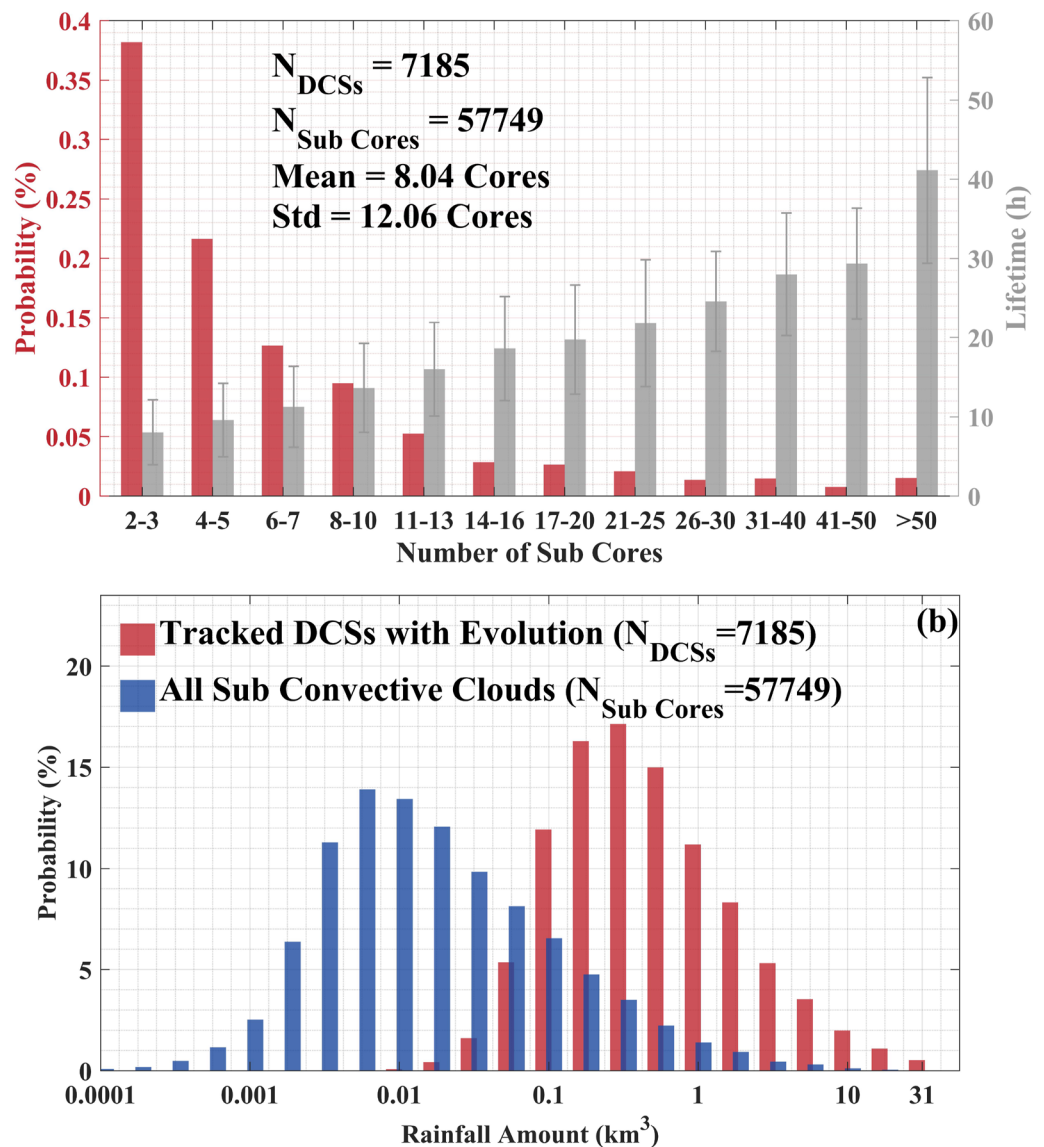


Figure 8. Characteristics of tracked deep convective systems (DCSs) with splitting evolution during their lifetime. The (a) show the probability distribution and related lifetime of DCSs with different numbers of sub-cores. The grey I-type vertical bars indicate the standard deviation of DCS lifetime. The (b) shows the comparison of rainfall amount probability distribution between these full DCSs and their sub-cores, which are not integrated with consideration of splits and mergers evolutions.

4. Summary and Conclusions

DCSs play a crucial role in the water cycle and Earth-atmosphere energy budget, especially in the tropics. However, capturing and quantifying the full lifecycle of DCS evolution and composition represents a great challenge due to the complicated processes of a DCS throughout its lifetime. Additionally, the whole DCS radiative forcing and related variations are determined by its whole coverage area and lifetime, especially for anvil and cirrus (Christensen et al., 2016; Feng et al., 2011; Hartmann & Berry, 2017). New requirements are raised about accurate tracking the whole full and components (core, anvil, and cirrus) of DCSs from their initial to total dissipation. Here, a method called FACTS is developed to identify and track the full lifetime and components of DCS

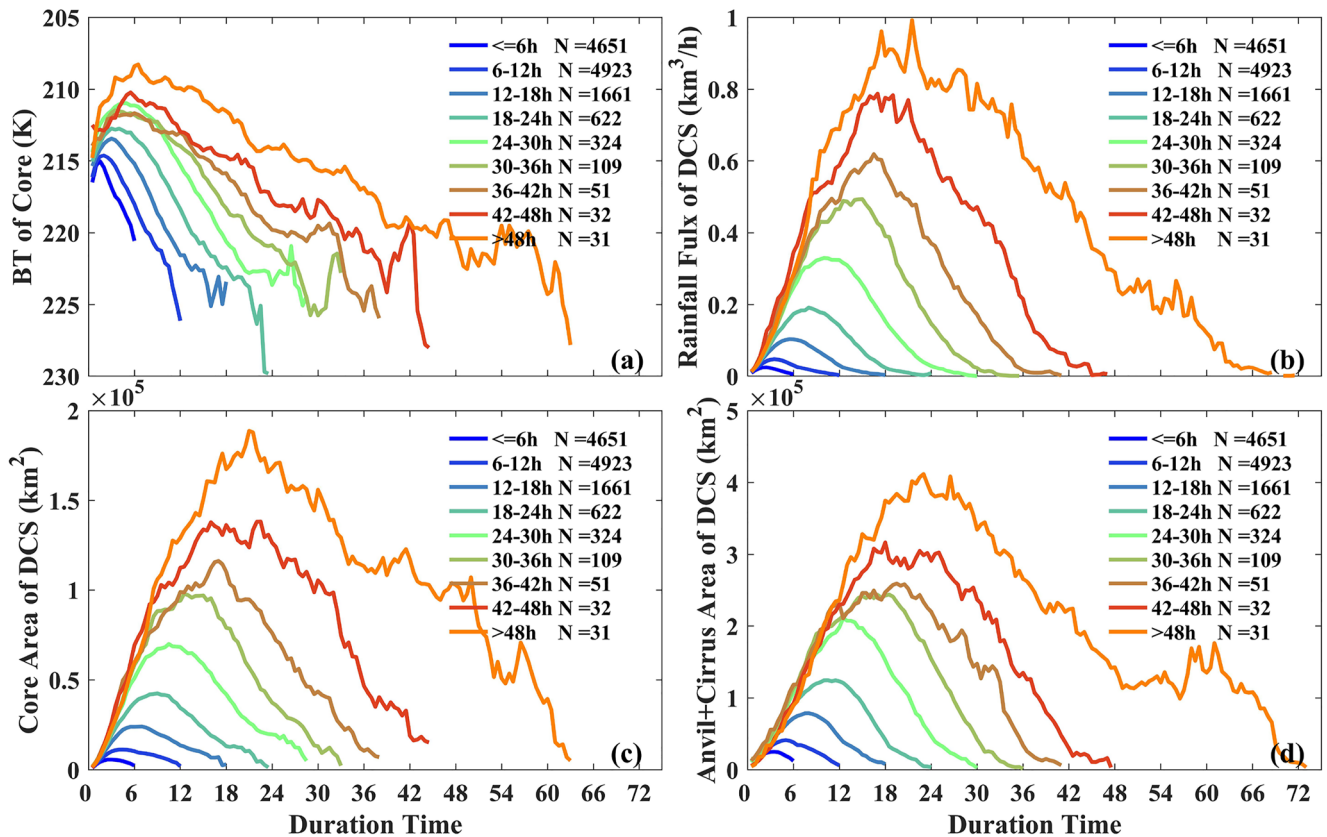


Figure 9. Evolution of deep convective system (DCS) characteristics at 6 hr lifetime intervals, including (a) the BT of core (12 μm), (b) the rainfall flux of DCS, (c) core area, and (d) the sum of anvil and cirrus areas. The rainfall flux of DCS is equal to rainfall rate times area.

including the splitting and merging evolution and the detrained cirrus throughout the DCS lifetime. Tracking DCS over the tropics in 2012 resulted in the following main conclusions:

1. Compared with the situation without considering splitting and merging evolutions, more than half of tracked DCSs experience splitting with an average of 8 sub-cores during their lifetime and a maximum of 100. Moreover, DCSs with a short lifetime are more likely without splitting in their lifetime.
2. A DCS is not identified as dissipated until all related cirrus detrained from this DCS are dissipated. By continuously tracking for detrained cirrus, DCSs lifetime are lengthened by up to 10 hr, and their area are enlarged by 16% on average, which is essential in radiative forcing calculations.
3. Long-lived DCSs generally have lower core BT, greater rainfall, and area, but lower frequency than short-lived DCSs. Although the rainfall amount of DCS substantially increases with lifetime, the integrated rainfall amount for DCSs at different lifetime bins are comparable.
4. DCS always develop to their greatest height at 1–6 hr after its initiation. However, rainfall flux and area always reach their peak near half of the lifetime, whereas maximum rainfall flux occurs slightly before the maximum area.

In this paper, a new DCS life cycle algorithm is developed from initial core to total dissipation of cirrus detrained from DCS, and all ice-top clouds split from the ancestor convective core will belong to the same DCS, including multiple sub-convective clouds and detrained cirrus. The FACTS method can successfully track the full evolution and all components of DCS (core, anvil, and cirrus) during its entire lifetime, enabling its application for understanding and quantifying the aerosols-DCS interaction and the effect of DCS on the Earth's radiative forcing more deeply and accurately in the future.

Conflict of Interest

The authors declare no conflicts of interest relevant to this study.

Data Availability Statement

The authors thank the science teams for providing excellent, accessible data, including MSG (<https://archive.eumetsat.int/>), Schmetz et al. (2002)), GPM (<https://arthurhou.pps.eosdis.nasa.gov/>, Hou et al., 2014), and NCEP (<https://rda.ucar.edu/datasets/ds083.2/>, Saha et al., 2010) reanalysis datasets. The data set about the properties of all captured complete deep convection cases is available at https://figshare.com/articles/dataset/DCS_Lifetime_Properties_to_JGR/21082099.

Acknowledgments

This paper is supported by the National Natural Science Foundation of China (41971285 and 41627804) and the Wuhan University Specific Fund for Major School-level Internationalization Initiatives. Numerical calculations in this paper are performed on the supercomputing system in the Supercomputing Center of Wuhan University.

References

- Ai, Y., Li, W., Meng, Z., & Li, J. (2016). Life cycle characteristics of MCSs in middle East China tracked by geostationary satellite and precipitation estimates. *Monthly Weather Review*, *144*(7), 2517–2530. <https://doi.org/10.1175/mwr-d-15-0197.1>
- Carey, L. D., Murphy, M. J., McCormick, T. L., & Demetriades, N. W. (2005). Lightning location relative to storm structure in a leading-line, trailing-stratiform mesoscale convective system. *Journal of Geophysical Research: Atmospheres*, *110*(D3). <https://doi.org/10.1029/2003jd004371>
- Carvalho, D., Rocha, A., Gómez-Gesteira, M., & Santos, C. S. (2014). WRF wind simulation and wind energy production estimates forced by different reanalyses: Comparison with observed data for Portugal. *Applied Energy*, *117*, 116–126. <https://doi.org/10.1016/j.apenergy.2013.12.001>
- Carvalho, L. M., Jones, C., & Liebmann, B. (2002). Extreme precipitation events in southeastern South America and large-scale convective patterns in the South Atlantic convergence zone. *Journal of Climate*, *15*(17), 2377–2394. [https://doi.org/10.1175/1520-0442\(2002\)015<2377:epeiss>2.0.co;2](https://doi.org/10.1175/1520-0442(2002)015<2377:epeiss>2.0.co;2)
- Chen, D., Guo, J., Yao, D., Lin, Y., Zhao, C., & Min, M. (2019). Mesoscale convective systems in the Asian monsoon region from Advanced Himawari Imager: Algorithms and preliminary results. *Journal of Geophysical Research: Atmospheres*, *124*(4), 2210–2234. <https://doi.org/10.1029/2018jd029707>
- Christensen, M. W., Chen, Y. C., & Stephens, G. L. (2016). Aerosol indirect effect dictated by liquid clouds. *Journal of Geophysical Research: Atmospheres*, *121*(24), 14636–14650. <https://doi.org/10.1002/2016jd025245>
- Cui, W., Dong, X., Xi, B., Feng, Z., & Fan, J. (2020). Can the GPM IMERG final product accurately represent MCSs' precipitation characteristics over the central and eastern United States? *Journal of Hydrometeorology*, *21*(1), 39–57.
- del Moral, A., Rigo, T., & Llasat, M. C. (2018). A radar-based centroid tracking algorithm for severe weather surveillance: Identifying split/merge processes in convective systems. *Atmospheric Research*, *213*, 110–120. <https://doi.org/10.1175/jhm-d-19-0123.1>
- Dixon, M., & Wiener, G. (1993). TITAN: Thunderstorm identification, tracking, analysis, and nowcasting—A radar-based methodology. *Journal of Atmospheric and Oceanic Technology*, *10*(6), 785–797. [https://doi.org/10.1175/1520-0426\(1993\)010<0785:titaat>2.0.co;2](https://doi.org/10.1175/1520-0426(1993)010<0785:titaat>2.0.co;2)
- Dong, Y., Li, G., Yuan, M., & Xie, X. (2017). Evaluation of five grid data sets against radiosonde data over the eastern and downstream regions of the Tibetan Plateau in summer. *Atmosphere*, *8*(3), 56. <https://doi.org/10.3390/atmos8030056>
- Feng, Z., Dong, X., Xi, B., McFarlane, S. A., Kennedy, A., Lin, B., & Minnis, P. (2012). Life cycle of midlatitude deep convective systems in a Lagrangian framework. *Journal of Geophysical Research: Atmospheres*, *117*(D23). <https://doi.org/10.1029/2012jd018362>
- Feng, Z., Dong, X., Xi, B., Schumacher, C., Minnis, P., & Khaiyer, M. (2011). Top-of-atmosphere radiation budget of convective core/stratiform rain and anvil clouds from deep convective systems. *Journal of Geophysical Research: Atmospheres*, *116*(D23). <https://doi.org/10.1029/2011jd016451>
- Feng, Z., Leung, L. R., Houze, R. A., Jr., Hagos, S., Hardin, J., Yang, Q., et al. (2018). Structure and evolution of mesoscale convective systems: Sensitivity to cloud microphysics in convection-permitting simulations over the United States. *Journal of Advances in Modeling Earth Systems*, *10*(7), 1470–1494. <https://doi.org/10.1029/2018ms001305>
- Feng, Z., Leung, L. R., Liu, N., Wang, J., Houze, R. A., Jr., Li, J., et al. (2021). A global high-resolution mesoscale convective system database using satellite-derived cloud tops, surface precipitation, and tracking. *Journal of Geophysical Research: Atmospheres*, *126*(8), e2020JD034202. <https://doi.org/10.1029/2020jd034202>
- Fioleau, T., & Roca, R. (2013). An algorithm for the detection and tracking of tropical mesoscale convective systems using infrared images from geostationary satellite. *IEEE Transactions on Geoscience and Remote Sensing*, *51*(7), 4302–4315. <https://doi.org/10.1109/tgrs.2012.2227762>
- Goyens, C., Lauwaet, D., Schröder, M., Demuzere, M., & Van Lipzig, N. P. (2012). Tracking mesoscale convective systems in the Sahel: Relation between cloud parameters and precipitation. *International Journal of Climatology*, *32*(12), 1921–1934. <https://doi.org/10.1002/joc.2407>
- Hall, D. L. (2004). Mathematical techniques in multisensor data fusion.
- Han, L., Fu, S., Zhao, L., Zheng, Y., Wang, H., & Lin, Y. (2009). 3D convective storm identification, tracking, and forecasting—An enhanced TITAN algorithm. *Journal of Atmospheric and Oceanic Technology*, *26*(4), 719–732. <https://doi.org/10.1175/2008jtecha1084.1>
- Hanna, J. W., Schultz, D. M., & Irving, A. R. (2008). Cloud top temperatures for precipitating winter clouds. *Journal of Applied Meteorology and Climatology*, *47*(1), 351–359. <https://doi.org/10.1175/2007jamec1549.1>
- Hartmann, D. L., & Berry, S. E. (2017). The balanced radiative effect of tropical anvil clouds. *Journal of Geophysical Research: Atmospheres*, *122*(9), 5003–5020. <https://doi.org/10.1002/2017jd026460>
- Hayden, L., & Liu, C. (2021). Differences in the diurnal variation of precipitation estimated by spaceborne radar, passive microwave radiometer, and IMERG. *Journal of Geophysical Research: Atmospheres*, *126*(9), e2020JD033020. <https://doi.org/10.1029/2020jd033020>
- Hennon, C. C., Helms, C. N., Knapp, K. R., & Bowen, A. R. (2011). An objective algorithm for detecting and tracking tropical cloud clusters: Implications for tropical cyclogenesis prediction. *Journal of Atmospheric and Oceanic Technology*, *28*(8), 1007–1018. <https://doi.org/10.1175/2010jtecha1522.1>
- Hou, A. Y., Kakar, R. K., Neeck, S., Azarbarzin, A. A., Kummerow, C. D., Kojima, M., et al. (2014). The global precipitation measurement mission. *Bulletin of the American Meteorological Society*, *95*(5), 701–722. <https://doi.org/10.1175/bams-d-13-00164.1>
- Hu, J., Rosenfeld, D., Ryzhkov, A., Zrnic, D., Williams, E., Zhang, P., et al. (2019). Polarimetric radar convective cell tracking reveals large sensitivity of cloud precipitation and electrification properties to CCN. *Journal of Geophysical Research: Atmospheres*, *124*(22), 12194–12205. <https://doi.org/10.1029/2019jd030857>

- Hu, J., Rosenfeld, D., Zrnic, D., Williams, E., Zhang, P., Snyder, J. C., et al. (2019). Tracking and characterization of convective cells through their maturation into stratiform storm elements using polarimetric radar and lightning detection. *Atmospheric Research*, 226, 192–207. <https://doi.org/10.1016/j.atmosres.2019.04.015>
- Huang, X., Hu, C., Huang, X., Chu, Y., Tseng, Y.-h., Zhang, G. J., & Lin, Y. (2018). A long-term tropical mesoscale convective systems data set based on a novel objective automatic tracking algorithm. *Climate Dynamics*, 51(7), 3145–3159. <https://doi.org/10.1007/s00382-018-4071-0>
- Huffman, G. J., Bolvin, D. T., Braithwaite, D., Hsu, K., Joyce, R., Xie, P., & Yoo, S. (2019). *Algorithm theoretical basis document (ATBD) version 06*. NASA Global Precipitation Measurement (GPM) Integrated Multi-Satellite Retrievals for GPM (IMERG), NASA. Retrieved from <https://pmm.nasa.gov/data-access/downloads/gpm>
- Huffman, G. J., Bolvin, D. T., Nelkin, E. J., Wolff, D. B., Adler, R. F., & Gu, G. (2007). The TRMM multisatellite precipitation analysis (TMPA): Quasi-global, multiyear, combined-sensor precipitation estimates at fine scales. *Journal of Hydrometeorology*, 8(1), 38–55. <https://doi.org/10.1175/jhm560.1>
- Inoue, T. (1987). A cloud type classification with NOAA 7 split-window measurements. *Journal of Geophysical Research: Atmospheres*, 92(D4), 3991–4000. <https://doi.org/10.1029/jd092id04p03991>
- Inoue, T., Vila, D., Rajendran, K., Hamada, A., Wu, X., & Machado, L. A. (2009). Life cycle of deep convective systems over the eastern tropical Pacific observed by TRMM and GOES-W. *Journal of the Meteorological Society of Japan. Series II*, 87, 381–391. <https://doi.org/10.2151/jmsj.87a.381>
- Koren, I., Dagan, G., & Altaratz, O. (2014). From aerosol-limited to invigoration of warm convective clouds. *Science*, 344(6188), 1143–1146. <https://doi.org/10.1126/science.1252595>
- Kummerow, C. D., Hong, Y., Olson, W., Yang, S., Adler, R., McCollum, J., et al. (2001). The evolution of the Goddard Profiling Algorithm (GPROF) for rainfall estimation from passive microwave sensors. *Journal of Applied Meteorology*, 40(11), 1801–1820. [https://doi.org/10.1175/1520-0450\(2001\)040<1801:teotgp>2.0.co;2](https://doi.org/10.1175/1520-0450(2001)040<1801:teotgp>2.0.co;2)
- Kummerow, C. D., Randel, D. L., Kulie, M., Wang, N.-Y., Ferraro, R., Joseph Munchak, S., & Petkovic, V. (2015). The evolution of the Goddard profiling algorithm to a fully parametric scheme. *Journal of Atmospheric and Oceanic Technology*, 32(12), 2265–2280. <https://doi.org/10.1175/jtech-d-15-0039.1>
- Lee, Y.-K., Otkin, J. A., & Greenwald, T. J. (2014). Evaluating the accuracy of a high-resolution model simulation through comparison with MODIS observations. *Journal of Applied Meteorology and Climatology*, 53(4), 1046–1058. <https://doi.org/10.1175/jamc-d-13-0140.1>
- Li, L., Schmid, W., & Joss, J. (1995). Nowcasting of motion and growth of precipitation with radar over a complex orography. *Journal of Applied Meteorology and Climatology*, 34(6), 1286–1300.
- Li, W., Zhang, F., Yu, Y., Iwabuchi, H., Shen, Z., Wang, G., & Zhang, Y. (2021). The semi-diurnal cycle of deep convective systems over Eastern China and its surrounding seas in summer based on an automatic tracking algorithm. *Climate Dynamics*, 56(1), 357–379. <https://doi.org/10.1007/s00382-020-05474-1>
- Liu, C., & Zipser, E. J. (2015). The global distribution of largest, deepest, and most intense precipitation systems. *Geophysical Research Letters*, 42(9), 3591–3595. <https://doi.org/10.1002/2015gl063776>
- Mathon, V., & Laurent, H. (2001). Life cycle of Sahelian mesoscale convective cloud systems. *Quarterly Journal of the Royal Meteorological Society*, 127(572), 377–406. <https://doi.org/10.1002/qj.4971275208>
- Matus, A. V., & L'Ecuyer, T. S. (2017). The role of cloud phase in Earth's radiation budget. *Journal of Geophysical Research: Atmospheres*, 122(5), 2559–2578. <https://doi.org/10.1002/2016jd025951>
- Meyer, F. (1994). Topographic distance and watershed lines. *Signal Processing*, 38(1), 113–125. [https://doi.org/10.1016/0165-1684\(94\)90060-4](https://doi.org/10.1016/0165-1684(94)90060-4)
- Ocasio, K. M. N., Evans, J. L., & Young, G. S. (2020). Tracking mesoscale convective systems that are potential candidates for tropical cyclogenesis. *Monthly Weather Review*, 148(2), 655–669.
- Pan, Z., Mao, F., Rosenfeld, D., Zhu, Y., Zang, L., & Lu, X. (2022). Coarse sea spray inhibits lightning. *Nature Communications*, 13(1), 1–7. <https://doi.org/10.1038/s41467-022-31714-5>
- Pan, Z., Rosenfeld, D., Zhu, Y., Mao, F., Gong, W., Zang, L., & Lu, X. (2021). Observational quantification of aerosol invigoration for deep convective cloud lifecycle properties based on geostationary satellite. *Journal of Geophysical Research: Atmospheres*, 126(9), e2020JD034275. <https://doi.org/10.1029/2020jd034275>
- Platt, C. M. R., & Harshvardhan (1988). Temperature dependence of cirrus extinction: Implications for climate feedback. *Journal of Geophysical Research: Atmospheres*, 93(D9), 11051–11058. <https://doi.org/10.1029/jd093id09p11051>
- Prein, A. F., Liu, C., Ikeda, K., Trier, S. B., Rasmussen, R. M., Holland, G. J., & Clark, M. P. (2017). Increased rainfall volume from future convective storms in the US. *Nature Climate Change*, 7(12), 880–884. <https://doi.org/10.1038/s41558-017-0007-7>
- Rasmussen, K. L., Chaplin, M., Zuluaga, M., & Houze, R., Jr. (2016). Contribution of extreme convective storms to rainfall in South America. *Journal of Hydrometeorology*, 17(1), 353–367. <https://doi.org/10.1175/jhm-d-15-0067.1>
- Rickenbach, T. M. (1998). Cloud-top evolution of tropical oceanic squall lines from radar reflectivity and infrared satellite data. *Monthly Weather Review*, 127(12), 2951–2976.
- Rinehart, R., & Garvey, E. (1978). Three-dimensional storm motion detection by conventional weather radar. *Nature*, 273(5660), 287–289. <https://doi.org/10.1038/273287a0>
- Roca, R., Aublanc, J., Chambon, P., Fiolleau, T., & Viltard, N. (2014). Robust observational quantification of the contribution of mesoscale convective systems to rainfall in the tropics. *Journal of Climate*, 27(13), 4952–4958. <https://doi.org/10.1175/jcli-d-13-00628.1>
- Roca, R., Berges, J. C., Brogniez, H., Capderou, M., Chambon, P., Chomette, O., et al. (2010). On the water and energy cycles in the Tropics. *Comptes Rendus Geoscience*, 342(4–5), 390–402. <https://doi.org/10.1016/j.crte.2010.01.003>
- Rosenfeld, D. (1987). Objective method for analysis and tracking of convective cells as seen by radar. *Journal of Atmospheric and Oceanic Technology*, 4(3), 422–434. [https://doi.org/10.1175/1520-0426\(1987\)004<0422:omfaat>2.0.co;2](https://doi.org/10.1175/1520-0426(1987)004<0422:omfaat>2.0.co;2)
- Rosenfeld, D., Lohmann, U., Raga, G. B., O'Dowd, C. D., Kulmala, M., & Fuzzi, S. (2008). Flood or drought: How do aerosols affect precipitation? *Science*, 321(5894), 1309–1313. <https://doi.org/10.1126/science.1160606>
- Saha, S., Moorthi, S., Pan, H.-L., Wu, X., Wang, J., & Nadiga, S. (2010). The NCEP climate forecast system reanalysis. *Bulletin of the American Meteorological Society*, 91(8), 1015–1058. <https://doi.org/10.1175/2010bams3001.1>
- Sassen, K., Wang, Z., & Liu, D. (2009). Global distribution of cirrus clouds from CloudSat/Cloud-Aerosol Lidar and Infrared Pathfinder Satellite Observations (CALIPSO) measurements. *Journal of Geophysical Research: Atmospheres*, 113(D8), <https://doi.org/10.1029/2008JD009972>
- Schmetz, J., Pili, P., Tjemkes, S., Just, D., Kerkmann, J., Rota, S., & Ratier, A. (2002). An introduction to Meteosat second generation (MSG). *Bulletin of the American Meteorological Society*, 83(7), 977–992. [https://doi.org/10.1175/1520-0477\(2002\)083<0992:staitm>2.3.co;2](https://doi.org/10.1175/1520-0477(2002)083<0992:staitm>2.3.co;2)
- Sivan, C., Rakesh, V., Abhilash, S., & Mohanakumar, K. (2021). Evaluation of global reanalysis winds and high-resolution regional model outputs with the 205 MHz stratosphere-troposphere wind profiler radar observations. *Quarterly Journal of the Royal Meteorological Society*, 147(737), 2562–2579. <https://doi.org/10.1002/qj.4041>

- Strabala, K. I., Ackerman, S. A., & Menzel, W. P. (1994). Cloud properties inferred from 8–12 μm data. *Journal of Applied Meteorology and Climatology*, 33(2), 212–229. [https://doi.org/10.1175/1520-0450\(1994\)033<0212:cpifd>2.0.co;2](https://doi.org/10.1175/1520-0450(1994)033<0212:cpifd>2.0.co;2)
- Taylor, C. M., Belušić, D., Guichard, F., Parker, D. J., Vischel, T., & Bock, O. (2017). Frequency of extreme Sahelian storms tripled since 1982 in satellite observations. *Nature*, 544(7651), 475–478. <https://doi.org/10.1038/nature22069>
- Tuttle, J. D., & Foote, G. B. (1990). Determination of the boundary layer airflow from a single Doppler radar. *Journal of Atmospheric and Oceanic Technology*, 7(2), 218–232. [https://doi.org/10.1175/1520-0426\(1990\)007<0218:dotbla>2.0.co;2](https://doi.org/10.1175/1520-0426(1990)007<0218:dotbla>2.0.co;2)
- Vila, D. A., Machado, L. A. T., Laurent, H., & Velasco, I. (2008). Forecast and Tracking the Evolution of Cloud Clusters (ForTraCC) using satellite infrared imagery: Methodology and validation. *Weather and Forecasting*, 23(2), 233–245. <https://doi.org/10.1175/2007waf2006121.1>
- Vondou, D. A., Nzeukou, A., & Kanga, F. M. (2010). Diurnal cycle of convective activity over the West of Central Africa based on Meteosat images. *International Journal of Applied Earth Observation and Geoinformation*, 12, S58–S62. <https://doi.org/10.1016/j.jag.2009.09.011>
- Wang, G., Wong, W., Liu, L., & Wang, H. (2013). Application of multi-scale tracking radar echoes scheme in quantitative precipitation nowcasting. *Advances in Atmospheric Sciences*, 30(2), 448–460. <https://doi.org/10.1007/s00376-012-2026-7>
- Wang, K. Y., & Liao, S. A. (2006). Lightning, radar reflectivity, infrared brightness temperature, and surface rainfall during the 2–4 July 2004 severe convective system over Taiwan area. *Journal of Geophysical Research: Atmospheres*, 111(D5). <https://doi.org/10.1029/2005jd006411>
- Whitehall, K., Mattmann, C. A., Jenkins, G., Rwebangira, M., Demoz, B., & Waliser, D. (2015). Exploring a graph theory based algorithm for automated identification and characterization of large mesoscale convective systems in satellite data sets. *Earth Science Informatics*, 8(3), 663–675. <https://doi.org/10.1007/s12145-014-0181-3>
- Williams, M., & Houze, R. A., Jr. (1987). Satellite-observed characteristics of winter monsoon cloud clusters. *Monthly Weather Review*, 115(2), 505–519. [https://doi.org/10.1175/1520-0493\(1987\)115<0505:socowm>2.0.co;2](https://doi.org/10.1175/1520-0493(1987)115<0505:socowm>2.0.co;2)
- Zan, B., Yu, Y., Li, J., Zhao, G., Zhang, T., & Ge, J. (2019). Solving the storm split-merge problem—A combined storm identification, tracking algorithm. *Atmospheric Research*, 218, 335–346. <https://doi.org/10.1016/j.atmosres.2018.12.007>
- Zhang, X., Shen, W., Zhuge, X., Yang, S., Chen, Y., & Wang, Y. (2021). Statistical characteristics of mesoscale convective systems initiated over the Tibetan Plateau in summer by Fengyun satellite and precipitation estimates. *Remote Sensing*, 13(9), 1652. <https://doi.org/10.3390/rs13091652>
- Zheng, J., Liu, D., Wang, Z., & Wang, Y. (2018). Differences among three types of tropical deep convective clusters observed from A-Train satellites. *Journal of Quantitative Spectroscopy and Radiative Transfer*, 217, 253–261. <https://doi.org/10.1016/j.jqsrt.2018.05.006>